Journal of The Electrochemical Society

OPEN ACCESS

Pathways Toward High-energy Li-sulfur Batteries, Identified via Multi-reaction Chemical Modeling

Journal of The Electrochemical Society, 2022 **169** 010520

Pathways Toward High-energy Li-sulfur Batteries, Identified via Multi-reaction Chemical Modeling

Daniel Korff,[1] Andrew M. Colclasure,[2] Yeyoung Ha,[2] Kandler A. Smith,[2] and Steven C. DeCaluwe[1,*,z]

[1]*Department of Mechanical Engineering, Colorado School of Mines, Golden, Colorado 80401, United States of America*
[2]*National Renewable Energy Laboratory, Golden, Colorado 80401, United States of America*

Here we present a 1D model of a Li-Sulfur battery with physically derived geometric parameters and thermodynamically consistent electrochemical kinetics. The approach enables straightforward comparison of proposed Li-S mechanisms and provides insights into the influence of polysulfide intermediates on battery discharge. Comparing predictions from multiple mechanisms demonstrates the need for both lithiated and non-lithiated polysulfide species, and highlights the challenge of developing parameter estimates for complex electrochemical mechanisms. The model is also used to explore cathode design strategies. Discharge performance and polysulfide concentrations for electrolyte/sulfur ratios in the range 2–4 μL mg^{-1} identifies trade-offs that limit battery energy and power density, and highlights the risk of polysulfide precipitation. New cathode and electrolyte approaches must limit polysulfide concentrations in the electrolyte, both to unlock better rate capabilities in Li-S technology and to prevent capacity fade due to polysulfide precipitation.
 [DOI: 10.1149/1945-7111/ac4541]

Manuscript submitted September 23, 2021; revised manuscript received November 22, 2021. Published January 18, 2022.

Supplementary material for this article is available online

Lithium-sulfur (Li-S) batteries are a promising "beyond Li-ion" technology, leveraging sulfur's high specific capacity (approximately 1675 Ah/kg$_{sulfur}$) and natural abundance to produce lighter, cheaper batteries. However, Li-S battery commercialization is limited by material properties which reduce performance and durability. Namely, the low conductivities of the charge and discharge end-states (S_8 and Li_2S, respectively), volumetric expansion during discharging from S_8 to Li_2S, and low cell potentials all limit performance.[1–3]

In addition to these issues, polysulfide intermediate species solubility in liquid electrolytes limits performance and durability. The so-called "polysulfide shuttling" of soluble intermediates and the precipitation of low-solubility intermediates can cause capacity fade, depending on the spatial distribution of electrolyte chemical composition.[3–7] Further, high electrolyte viscosity with high polysulfide concentrations prevents high-rate battery cycling.[8–10] It is therefore necessary, for future Li-S battery and electrolyte designs, to understand and control electrolyte speciation to optimize performance while minimizing capacity fade.[11–14]

This work models the detailed thermo- and electro-chemistry of Li-S batteries to understand the impact of intermediate species concentrations on performance. Recent models have described new approaches for improved model accuracy or flexibility, for insight into limiting phenomena. These efforts originate with the 1D model by Kumaresan et al.,[15] which models the discharge mechanism via a simple linear cascade of polysfulides S_n^{2-} with decreasing order n. Subsequent extensions of this model have examined the influence of solid active phases on predicted behavior,[2] implemented nucleation and growth mechanisms to demonstrate the impact of discharge rate and lithium sulfide morphology,[16,17] and added shuttling induced capacity loss.[6] Zhang et al. demonstrated the ability to recover capacity lost due to transport limitations by relaxing cells after high-current discharge.[18] Hofmann et al. investigated reduced order mechanisms to capture major performance features,[19] but Schön and Krewer used cyclic voltammetry (CV) to demonstrate the importance of detailed mechanisms to capture certain features.[20]

These previous models provide valuable insights into limiting phenomena, but additional chemical complexity is typically not considered. The implemented reaction mechanisms are usually based on that from Kumaresan et al.[15] In particular, these mechanisms treat the intermediate polysulfide species as "non-lithiated": the polysulfide anion remains fully dissociated from Li^+ cations and is fully solvated by the electrolyte solvent. However, atomistic calculations and *operando* measurements suggest the favorability of a "lithiated" pathway.[21–23] This lithiated pathway assumes aggregate solvation structures or bonds between the Li^+ and the sulfur anions. Others have shown that ion concentrations and the electrolyte composition can influence polysulfide solubility or dissolution behavior.[24–27] Simulations by Parke et al., included a dissociation reaction to form $S_3^{\bullet-}$, demonstrating its notable impact on predicted performance.[28] CV experiments by Thangavel et al. support this claim.[29]

In this paper, we use detailed thermo-kinetic modeling of Li-S battery performance to understand the role of multi-reaction chemical pathways on battery performance and degradation. The model presented implements a mechanism based on work by Neidhardt et al.,[30] supplemented with additional mechanisms derived from DFT and quantum chemical calculations.[22,23] Using the open-source chemical software Cantera,[31] we develop a 1D, single-cell simulation tool that incorporates chemical mechanisms of varying complexity. This tool is used to predict battery performance, examined simultaneously with the concentration and distribution of reaction intermediates. The results are validated against previous experimental data, and establish the need for additional detailed thermo-kinetic mechanism information (thermodynamic and kinetic parameters). Finally, the simulation results provide guidance for next-generation Li-S battery design. By examining power vs energy densities (i.e. Ragone plots) within the context of species solubility limits, we identify design pathways to balance gravimetric performance with low degradation rates.

Model Formulation

The isothermal model presented here is written as a set of physically-derived conservation equations, discretized in one dimension with a finite volume approach, and integrated as a function of time during galvanostatic discharge of the single-cell battery. The model implements balance equations for mass, species, and charge which constitute a set of differential algebraic equations (DAE). The model is written in Python,[32] using the software package Assimulo[33] to integrate the DAE set, and using Cantera[31] to manage species

*Electrochemical Society Member.
[z]E-mail: decaluwe@mines.edu

and phase thermochemical property calculations. A single discharge curve typically takes 30–60 min to run on an Intel i7-9750H processor, depending on the mechanism used and the C-rate. In this section, we present the model formulation, including balance equations, boundary and initial conditions, and model parameters.

Model Domain.—The 1D model domain, shown schematically in Fig. 1, includes a dense Li metal anode, porous electrolyte separator, and porous carbon-sulfur cathode. The latter two components are flooded with liquid electrolyte, 1M LiTFSI (lithium bis (trifluoromethanesulfonyl)imide) salt in a TEGDME (tetraethylene glycol dimethyl ether) solvent. The cathode is composed of a conductive carbon host, in which the sulfur is infiltrated.[4] The model represents the cathode as a series of spherical carbon particles, upon which representative hemispheres of the solid charge and discharge products (S_8 and Li_2S, respectively) precipitate. During discharge, the solid S_8 dissolves into the electrolyte, where it is reduced at the carbon/electrolyte interface to form lower-order polysulfides. These polysulfides are further reduced to eventually form solid Li_2S. As illustrated in Fig. 1, the model examines two reduction mechanism classes, one where the polysulfides are non-lithiated and one where they are lithiated. The anode is treated as ideal, and acts as the reservoir for Li^+ in the cell. A constant current boundary condition is imposed at the current collector for both electrodes. The model results below focus solely on discharge, although the model is capable of both charge and discharge.

Governing equations.—The battery's state at a given location is fixed by the following variables:

In the cathode:

- ε_{S_8}, volume fraction of solid sulfur (-)
- ε_{Li_2S}, volume fraction of solid lithium sulfide (-)
- $C_{k,\text{elyte}}$, molar concentration of species k in the electrolyte phase ($\text{kmol}_k\ \text{m}^{-3}_{\text{elyte}}$)
- ϕ_{carbon}, the electric potential of the cathode carbon phase (V)
- ϕ_{elyte}, the electric potential of the electrolyte phase (V)

In the electrolyte separator:

- $C_{k,\text{elyte}}$, molar concentration of electrolyte species k ($\text{kmol}_k\ \text{m}^{-3}_{\text{elyte}}$)
- ϕ_{elyte}, the electric potential of the electrolyte phase (V)

In the anode:

- $C_{k,\text{elyte}}$, molar concentration of electrolyte species k at the anode surface ($\text{kmol}_k\ \text{m}^{-3}_{\text{elyte}}$)
- ϕ_{elyte}, the electric potential of the electrolyte phase at the anode surface (V)
- ϕ_{Li}, the electric potential of the metallic Li anode phase (V)

The evolution of these variables during battery operation is predicted via governing equations derived from physically-based conservation equations for the mass, elements, and electrical charge:

Solid phase volume fractions.—For the cathode solid-phase end states—solid S_8 in the charged state and solid Li_2S in the discharged state—constant mass density of each phase (kg per m^3 of phase) is assumed. As such, conservation of mass leads to the following for ε_m, the volume fraction of the solid phase m (sulfur or lithium sulfide):

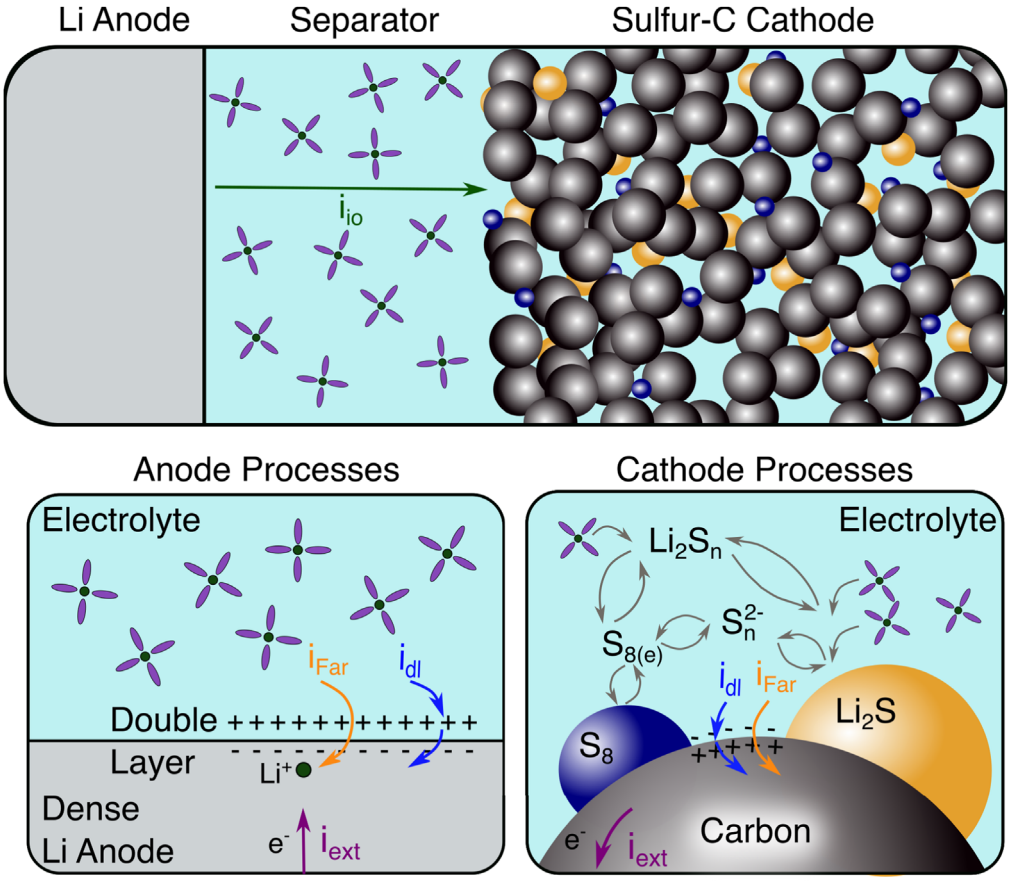

Figure 1. Illustration of model domain and electrode processes. The simulation includes an ideal Li metal anode, a porous electrolyte separator and a porous carbon cathode host, flooded with liquid electrolyte (1M LiTFSI in TEGDME). In the porous cathode, two chemical pathways between S_8 and Li_2S are examined, wherein the dissolved polysulfides are either lithiated or non-lithiated. Charge transfer reactions (Faradaic current and double-layer charging current) occur at the Li/electrolyte and carbon/electrolyte interfaces in the anode and cathode, respectively.

$$\frac{\partial \varepsilon_m}{\partial t} = a_m \sum_k \bar{v}_k \dot{s}_k, \quad [1]$$

where $\bar{v}_k$ is the constant molar volume (m^3 $kmol_k^{-1}$, equal to molecular weight divided by mass density) and $\dot{s}_k$ the molar production rate due to heterogeneous reactions ($kmol_k$ m^{-2} s^{-1}) for species k in phase m. The parameter a_m is the volume-specific area (m^{-1}) of the interface between phase m and the electrolyte for either of the bulk phases whose volume fractions vary during discharge (sulfur or lithium sulfide).

Electrolyte species.—The concentration of the electrolyte species k in the porous cathode and electrolyte separator varies with time due to chemical and electrochemical reactions, species transport, and the change in electrolyte volume fraction due to changing solid phase volume fractions. Conservation of mass and elements are combined to derive a differential equation for the species molar concentration (per unit volume of electrolyte phase).

$$\frac{\partial C_{k,\text{elyte}}}{\partial t} = \frac{1}{\varepsilon_{\text{elyte}}}\left(\sum_m a_m \dot{s}_{k,\text{elyte}} - \nabla N_{k,\text{elyte}}\right) + \dot{\omega}_{k,\text{elyte}} - \frac{C_{k,\text{elyte}}}{\varepsilon_{\text{elyte}}}\frac{\partial \varepsilon_{\text{elyte}}}{\partial t}, \quad [2]$$

where $\dot{\omega}_{k,\text{elyte}}$ is the molar production rate of species k due to homogeneous electrolyte phase reactions ($kmol_k$ m_{elyte}^{-3} s^{-1}) and $N_{k,\text{elyte}}$ is the molar flux of electrolyte species k ($kmol_k$ m^{-2} s^{-1}). In the electrolyte separator there are no surface reactions ($a_m \dot{s}_{k,\text{elyte}} = 0$), and homogeneous reactions are neglected throughout the modeling domain ($\dot{\omega}_{k,\text{elyte}} = 0$), for the present work. The rate of change of the electrolyte volume fraction $\left(\frac{\partial \varepsilon_{\text{elyte}}}{\partial t}\right)$ in the porous cathode is calculated as:

$$\frac{\partial \varepsilon_{\text{elyte}}}{\partial t} = -\frac{\partial \varepsilon_{S_8}}{\partial t} - \frac{\partial \varepsilon_{Li_2S}}{\partial t}, \quad [3]$$

where solid phase volume fraction rates of change are calculated via Eq. 1. The electrolyte treatment makes two primary assumptions: that convective flux is negligible and that the total cell volume is constant (i.e. the electrolyte is compressible with no pressure effects). Here, the assumed compressibility compensates for unmodeled convection effects in a qualitatively consistent manner, as concentration gradients will favor diffusion toward low concentration regions. According to Danner and Latz, convective transport has a minor effect on fluxes.[17] Future work will implement species convection effects and compressibility considerations.

Phase electric potentials.—Within the cathode, the electrolyte and cathode carbon phase electric potentials are solved by applying conservation of charge and assuming charge neutrality. Charge neutrality in the electrolyte phase of a given volume implies that the sum of all currents into the volume equals zero:

$$\nabla i_{\text{io}} + i_{\text{Far,ca}} + i_{\text{dl,ca}} = 0, \quad [4]$$

where i_{io} is the electrolyte phase ionic current density (A m^{-2}), $i_{\text{Far,ca}}$ the Faradaic charge transfer current per unit volume (A m^{-3}), and $i_{\text{dl,ca}}$ the local double-layer current per unit volume (A m^{-3}). $i_{\text{Far,ca}}$ and $i_{\text{dl,ca}}$ are formulated such that positive current represents net positive charge transferred from the electrolyte to the solid electrode phase, as illustrated schematically in Fig. 1.

The ionic current in the electrolyte is a function of the species fluxes $N_{k,\text{elyte}}$:

$$i_{\text{io}} = F \sum_{k,\text{elyte}} z_k N_k, \quad [5]$$

where F is Faraday's constant and z_k is the elementary charge of species k. The double layer current, therefore, balances the residual of the sum of the remaining charge fluxes, transferring charge between the electrolyte bulk phase and the capacitive double layer at the electrolyte/electrode interface to maintain charge neutrality in the electrolyte bulk. Modeling the double layer as a capacitor with capacitance C_{dl} (F m^{-2}) links the rate of change of the double layer potential $\Delta\phi_{\text{dl}}$ to the double-layer current:

$$\frac{\partial \Delta\phi_{\text{dl}}}{\partial t} = -\frac{i_{\text{dl}}}{C_{\text{dl}}\, a_{\text{dl}}}, \quad [6]$$

where the double layer potential equals the difference between the electrode solid phase ("ed"–cathode or anode) and the bulk electrolyte ("elyte") phases:

$$\Delta\phi_{\text{dl}} = \phi_{\text{ed}} - \phi_{\text{elyte}}. \quad [7]$$

Charge conservation and charge neutrality are also applied to each volume as a whole to yield:

$$0 = \nabla i_{\text{io}} + \nabla i_{\text{el}}, \quad [8]$$

where i_{el} is the electronic current density (A m^{-2}), calculated via Ohm's Law. i_{io} is a function of $C_{k,\text{elyte}}$ and ϕ_{elyte}, while i_{el} is a function of ϕ_{ca} only. $C_{k,\text{elyte}}$ is governed by Eq. 2, therefore Eqs. 6–8 fix the electric potentials of the two phases throughout the domain. Equation 6 is a differential equation, integrated in time to solve the double layer potential $\Delta\phi_{\text{dl}}$, which determines the ϕ_{elyte} at any given time. Equation 8 is an algebraic equation that must be satisfied at any point in time by the ϕ_{ed} values in the cathode.

In the electrolyte separator, there is no electronic current, and so Eq. 8 reduces to:

$$0 = \nabla i_{\text{io}}, \quad [9]$$

with i_{io} calculated as in Eq. 5. Boundary conditions imply that $i_{\text{io}} = i_{\text{ext}}$, in the separator.

The anode is modeled as dense Li, with the electric potential resolved via a capacitive double layer at the electrolyte separator–anode boundary. Charge neutrality in the anode requires that all currents sum to zero:

$$i_{\text{ext}} + i_{\text{Far,an}} + i_{\text{dl,an}} = 0, \quad [10]$$

where all currents represent positive charge delivered to the bulk Li anode. i_{ext} represents the user-specified external current (positive current corresponds to battery discharge). As with the cathode, i_{dl} is used to calculate the rate of change of the anode–electrolyte double layer potential, via Eq. 6.

Process variables: reaction and transport rate calculations.— The charge-transfer reactions are evaluated using mass action kinetics and are handled by Cantera. The Cantera input file allows user specification of Arrhenius parameters (pre-exponential A, temperature exponent b, and activation energy E_a) and the charge-transfer symmetry factor β for the forward rate coefficient:

$$k_f = A T^b \exp\left(-\frac{E_a}{RT}\right)\exp\left(-\sum_k \frac{\beta \nu_k z_k \phi_k}{RT}\right). \quad [11]$$

Here, R is the universal gas constant, T the temperature, and ν_k, z_k, and ϕ_k are the net stoichiometric coefficient, elementary charge, and phase electric potential for species k, respectively. For non-charge-transfer reactions, the electric potential summation evaluates to zero,

and typical Arrhenius rate coefficients are recovered. The reverse rate coefficient k_r for each reaction is calculated as the reaction's equilibrium coefficient divided by the forward rate coefficient, to maintain thermodynamic consistency.[34]

For a reaction i, the net rate of progress $\dot{q}_i$ is

$$\dot{q}_i = k_{f,i} \prod_k C_{ac,k}^{\nu'_{k,i}} - k_{r,i} \prod_k C_{ac,k}^{\nu''_{k,i}}, \quad [12]$$

where $\nu'_{k,i}$ and $\nu''_{k,i}$ are the forward and reverse stoichiometric coefficients for species k in reaction i, respectively, and $C_{ac,k}$ is the "activity concentration" for species k (kmol m^{-3}). We use CANTERA's `ideal-condensed` thermo-phase class for the electrolyte phase and the `fixed-stoichiometry` class for all other phases. The former model, as implemented here, sets the activity concentrations equal to the mole fractions X_k, while the latter sets $C_{ac,k} = 1.0$ The net production rate for a given species due to a set of reactions ($\dot{s}_k$ or $\dot{\omega}_k$, above) is calculated by summing the product of $\dot{q}_i$ times the net stoichiometric coefficient for species k in reaction i, over all reactions.

Electrolyte transport calculations use the Poisson-Nernst-Planck equation and dilute solution approximation:

$$N_{k,elyte} = -D_k^{eff}\left(\nabla C_k + C_k \frac{z_k F}{RT} \nabla \phi_{elyte}\right), \quad [13]$$

where C_k is taken at the interface between adjacent volumes (via weighted averaging of the volume-center concentrations) and ∇C_k uses the finite difference in volume-center concentrations.

Multiple studies have documented electrolyte composition dependent transport properties in Li-S batteries.[8–10] As the ion concentration increases, so too does the electrolyte viscosity, impeding species transport. The time-dependent electrolyte resistance due to changing species concentrations is incorporated here via an empirical model based on work by Zhang et al.,[8] to calculate D_{Li^+} according to the function

$$D_{Li^+} = D^\circ_{Li^+} - b \times |C_{Li^+/Li} - C^\circ_{Li^+/Li}| \quad [14]$$

where $D^\circ_{Li^+}$ is the Li^+ diffusion coefficient at the simulation initial conditions, $b = 1 \times 10^{-11}$ (m^5 kmol^{-1} s^{-1}), and where $C_{Li^+/Li}$ and $C^\circ_{Li^+/Li}$ are the total and total initial lithium concentrations (sum of Li contained in Li^+ and any Li-polysulfides), respectively. Due to unknown concentration dependent transport properties of the intermediate polysulfide species, the effect is only considered for Li^+ transport, as in Zhang et al.[8] The effective diffusion coefficient D_k^{eff} incorporates the transient local microstructure:

$$D_k^{eff} = \frac{\varepsilon_{elyte}}{\tau_{fac}} D_k = D_k \varepsilon_{elyte}^{1.5} \quad [15]$$

where the bulk diffusion coefficient is D_k, and where we replace the local tortuosity factor τ_{fac} with a common Bruggeman correlation, $\tau_{fac} = \varepsilon_{elyte}^{-0.5}$.[35] Although Eq. 13 can accommodate the more accurate concentrated solution theory (CST),[36] the CST framework requires significant alteration to accomodate the multiple charged species in the Li-S system,[37] and is left for future work.

Initial conditions and geometric parameters.—Here, we describe the derivation of microstructural parameters from a small number of experimental/cell fabrication variables and physical constants:

- $m''^{,\circ}_{S_8}$, the initial mass loading of sulfur (kg m^{-2})
- ω°_m, the initial weight percent of each phase m (kg$_m$ kg$_{tot}^{-1}$)
- H_{ca}, the cathode thickness (m)
- ρ_m, the mass density of phase m, (kg$_m$ m$_m^{-3}$)

These input parameters allow calculation of the initial volume fraction of solid phases:

$$\varepsilon^\circ_{S_8} = \frac{m''^{,\circ}_{S_8}}{\rho_{S_8} H_{ca}} \quad [16]$$

$$\varepsilon^\circ_{carbon} = \frac{\omega^\circ_{carbon}}{\omega^\circ_{S_8}} \frac{m''^{,\circ}_{S_8}}{\rho_{carbon} H_{ca}} \quad [17]$$

$$\varepsilon^\circ_{elyte} = 1 - \varepsilon^\circ_{S_8} - \varepsilon^\circ_{carbon} - \varepsilon^\circ_{Li_2S} \quad [18]$$

The initial Li_2S is assumed very small (state of charge = 100%; $\varepsilon^\circ_{Li_2S} = 10^{-5}$). For the simulations presented in this work, the volume fraction of carbon, $\varepsilon^\circ_{carbon}$, is assumed to be 5.6%, based on experiments reported by Andrei, et al., used for validation in this study.[38]

Assuming hemispherical particles of active end products (S_8 and Li_2S) in the cathode, the volume-specific interface area of the active phases is derived using the following variables:

- r_m, radius of the representative hemisphere of phase m (m)
- a_m, volume specific interface area between phase m and the electrolyte (m^2_m m$_{tot}^{-3}$)
- n_m, the number of hemispheres of phase m, per unit volume (m$_{tot}^{-3}$)

Where n_m is assumed constant and r_m varies as ε_m changes.

Li_2S formation proceeds via heterogeneous nucleation and growth of Li_2S particles at the carbon/electrolyte interface, with the nuclei concentration dependent on the C-rate.[16] At low C-rates, fewer Li_2S nuclei form, which grow larger during discharge. At high C-rates a greater number of Li_2S nuclei tend to form, which can form a passivating film in extreme cases. The nucleation and growth phenomena therefore impact the interface area (a_m for solid sulfur and lithium sulfide, as well as the carbon-electrolyte interface, a_{carbon}) and porosity evolution during discharge. We capture this dependence via a semi-empirical function to relate the applied C-rate to the nucleation density n_m of the solid Li_2S in the cathode:

$$n_m = n^\circ_m \exp(2.4221 \times C) \quad [19]$$

where C is the user input C-rate. The pre-exponential n°_m is set to 5×10^{13} for high-porosity carbon nanotube cathodes, as in Andrei et al.[38] Simulations that follow the work of Kumaresan, et al., typically neglect the dependence of n_m on C-rate, leading to predictions that overestimate the battery capacity with increasing C-rate.[15] Future extensions of this work will directly implement heterogeneous nucleation and growth kinetics, for a physics-based understanding of solid phase morphology as a function of operating conditions.

One novel feature of this work is the method by which the active phase interface area is updated based on time-dependent volume fractions. Typically, an empirical expression is used, such as $a_m = a^\circ_m(\varepsilon_m/\varepsilon^\circ_m)^\xi$.[15,28,30] In this work, assuming hemispherical particles, the total interface area for phase m and the electrolyte per unit total volume of electrode is a function of the state variable ε_m and the (constant) number of particles n_m:

$$a_m = 2\pi n_m \left(\frac{3\varepsilon_m}{2\pi n_m}\right)^{2/3} \quad [20]$$

The active area of the carbon/electrolyte interface is calculated by assuming an intrinsic carbon surface area and then subtracting the area covered by the active phase hemispheres at any given time:

Table I. Species parameters and initial conditions for the "non-lithiated polysulfide" mechanism. For species k, h_k° is the standard-state molar enthalpy, D_k° the bulk-phase diffusion coefficient, and C^o_k is the initial molar concentration. For the current isothermal model, s_k° was assumed as 0.0 kJ mol^{-1} K^{-1}.

Species	h_k° (kJ mol^{-1})	D_k° (m^2 s^{-1})	C_k^o (kmol m^{-3})
Solid Cathode Species			
S_8(s)	0.0[a]		
Li_2S(s)	−1112.48[b]		
Liquid Electrolyte Species			
S_8(e)	16.1[b]	1×10^{-11}[a]	1.943×10^{-2} [30]
S_8^{2-}	−450.78[b]	6×10^{-11}[a]	1.821×10^{-4} [30]
S_6^{2-}	−445.15[b]	6×10^{-11}[a]	3.314×10^{-4} [30]
S_4^{2-}	−433.14[b]	1×10^{-10} [30]	2.046×10^{-5} [30]
S_2^{2-}	−401.82[b]	1×10^{-10} [30]	5.348×10^{-10} [30]
S^{2-}	−383.27[b]	1×10^{-10} [30]	8.456×10^{-13} [30]
Li^+	−278.0[19]	1×10^{-10} [30]	1.024[30]
$TFSI^-$	0.0[a]	4×10^{-10}[a]	1.0229[a]
TEGDME	0.0[a]	1×10^{-12}[a]	1.023×10^{1}[a]
Solid Anode Species			
Li(s)	0.0[a]		

a Assumed parameters. b fit parameters.

$$a_{\text{carbon}} = a^\circ_{\text{carbon}} - \sum_m n_m \pi r_m^2 \quad [21]$$

To facilitate reproduction and extension of this work, the source code for the model is available as an open source GitHub repository.[39] The simulation data and scripts used to create the figures for this manuscript are also publicly available.[40]

Results

Model results are presented below for four separate thermo-kinetic mechanisms. Two were developed as part of this work, derived from the thermo-kinetic parameters used by Neidhardt et al.,[30] and adjusted to match experimental data.[38] The parameters for these two mechanisms are detailed in Tables I–IV.

- "Non-lithiated polysulfides" (Tables I, II): This mechanism follows the typical form from previous continuum simulations, where reduction proceeds via a linear cascade of polysulfide anions S_n^{2-} of decreasing order n.
- "Lithiated polysulfides" (Tables III, IV): This mechanism includes the same species and reactions as the "non-lithiated" mechanism, but with all intermediate species defined as charge-neutral lithiated polysulfides Li_2S_n.

Future simulations combining lithiated and non-lithiated pathways will require estimates for the nearly 50 parameters in Tables I–IV. Even with detailed *operando* validation data, fitting this many parameters is not altogether feasible. Rather, simulations should leverage atomistic calculations. To demonstrate atomistic mechanism adoption, we also show results using thermodynamics adopted from studies by Assary et al.,[22] and Kuz'mina et al.,[23] as shown in Supplementary Tables S1 and S2 available online at stacks.iop.org/JES/169/010520/mmedia. Species thermodynamics are adopted wholesale, while kinetic parameters are fitted to agree with experimental data. For the sake of comparison, only a portion of the Assary mechanism is adopted, to keep all four mechanisms similar in size.

Below, we present results for two studies. First, we compare simulations for the four mechanisms to experimental data from Andrei et al.[38] These data were chosen for validation because of how thoroughly the paper documents the electrode fabrication parameters. These simulations assume an initial cathode porosity of 85% to match the experiments. In the subsequent section, we assume a more relevant cathode microstructure (increasing sulfur loading, which lowers initial porosity), and use the "lithiated polysulfide" mechanism to explore Li-S cathode design parameters. We demonstrate the predicted impact of varying the electrolyte/sulfur (E/S) ratio on the battery performance and polysulfide concentrations. "Capacity" in Figs. 2–5 refers to the discharged capacity at a given time based on the external current applied.

High-porosity simulations for model validation and comparison.—The models are validated by fitting the thermodynamic ("non-lithiated" and "lithiated") and kinetic parameters (all mechanisms) against discharge data from Andrei et al.,[38] at rates of 0.1C, 0.5C, and 1.0C. A subset of Cantera input parameters (h_k° and forward rate constant, indicated in Tables I–IV) were fit by hand, to maximize quality of fit to the experimental data. The sums of squared residuals (SSR) are provided for each mechanism, in Fig. 2. A sensitivity analysis of the fitted parameters for the 'lithiated' mechanism is presented in the Supplemental Information, which indicates that the species thermodynamic parameters are determined with high precision, but that the fit is less sensitive to the kinetic rate constants k_f. Geometric parameters are chosen to match the experiment and are given in Table V. Results, presented in Figs. 2a–2d, show that the two continuum models capture the discharge capacity

Table II. Kinetic parameters for the "non-lithiated polysulfide" mechanism.

Reaction	Forward rate constant	Units
Sulfur/electrolyte interface		
S_8(s) ⇌ S_8(e)	1.9×10^{-2}[b]	—
Carbon/electrolyte interface		
$\frac{1}{2}\,S_8$(e) + e^- ⇌ $\frac{1}{2}\,S_8^{2-}$	8.725×10^{16}[b]	kmol$^{0.5}$ m$^{-0.5}$ s^{-1}
$\frac{3}{2}\,S_8^{2-}$ + e^- ⇌ 2 S_6^{2-}	4.331×10^{17}[b]	kmol$^{-0.5}$ m$^{2.5}$ s^{-1}
S_6^{2-} + e^- ⇌ $\frac{3}{2}\,S_4^{2-}$	3.193×10^{15}[b]	m^1 s^{-1}
$\frac{1}{2}\,S_4^{2-}$ + e^- ⇌ S_2^{2-}	2.375×10^{12}[b]	kmol$^{0.5}$ m$^{-0.5}$ s^{-1}
$\frac{1}{2}\,S_2^{2-}$ + e^- ⇌ S^{2-}	8.655×10^{13}[b]	kmol$^{0.5}$ m$^{-0.5}$ s^{-1}
Li_2S(s)/electrolyte interface		
2 Li^+ + S^{2-} ⇌ Li_2S(s)	1.075[b]	kmol^{-2} m^7 s^{-1}
Li(s)/electrolyte interface		
Li(s) ⇌ Li^+ + e^-	3.0×10^{-8}[b]	kmol m^{-2} s^{-1}

a Assumed parameters. b fit parameters.

Table III. Species parameters and initial conditions for the "lithiated polysulfide" mechanism. For species k, h_k° is the standard-state molar enthalpy, D_k° the bulk-phase diffusion coefficient, and $C^o{}_k$ is the initial molar concentration. For the current isothermal model, s_k° was assumed as 0.0 kJ mol^{-1} K^{-1}.

Species	h_k° (kJ mol^{-1})	D_k° (m^2 s^{-1})	C_k° (kmol m^{-3})
Solid Cathode Species			
S_8(s)	0.0[a]		
Li_2S(s)	−1112.48[b]		
Liquid Electrolyte Species			
S_8(e)	16.1[b]	1×10^{-11}[a]	1.943×10^{-2} [30]
Li_2S_8	− 1006.78[b]	6×10^{-11}[a]	1.821×10^{-4} [30]
Li_2S_6	− 1004.15[b]	6×10^{-11}[a]	3.314×10^{-4} [30]
Li_2S_4	− 994.14[b]	1×10^{-10}[a]	2.046×10^{-5} [30]
Li_2S_2	− 963.82[b]	1×10^{-10}[a]	5.348×10^{-10} [30]
Li_2S(e)	− 941.27[b]	1×10^{-10}[a]	8.456×10^{-13} [30]
Li^+	− 278.0[19]	1×10^{-10} [30]	1.024[30]
$TFSI^-$	0.0[a]	4×10^{-10}[a]	1.024[a]
TEGDME	0.0[a]	1×10^{-12}[a]	1.023×10^{1}[a]
Solid Anode Species			
Li(s)	0.0[a]		

a Assumed parameters. b fit parameters.

rate dependence and major discharge profile features. The mechanism using lithiated polysulfides provides a slightly better fit, particularly to the shape of the lower voltage plateau, but under-predicts the voltage at higher C-rates. This under-prediction of the voltage plateau is likely due to the increasing impact of poorly understood kinetic rate parameters on cell performance at higher C-rate discharge. Additionally, there may be elements of mechanism complexity not modeled here that become more important at higher C-rates. Examining the transition between upper and lower voltage plateaus, there is reasonable agreement, but the cell potential minimum or "dip" occurs at a higher capacity than in the experimental data. This dip is associated with the onset of solid Li_2S formation[30,38] in conjunction with increasing concentrations of Li_2S in the electrolyte (and associated electrolyte transport limitations).

Implementing multiple reaction mechanisms in a common model framework allows for direct comparisons between them. The two continuum-derived models ("non-lithiated" and "lithiated" polysulfides) predict similar discharge curves (Figs. 2a, 2b), but with minor differences. The polysulfide concentrations (Figs. 2e, 2f) demonstrate that these are linked to intermediate species concentrations, which we explore in detail, below.

The two atomistic-derived mechanisms in Figs. 2c and 2d demonstrate that, while theory provides valuable input for mechanism development, work remains to "tune" these mechanisms for accurate predictions. The best fits show discrepancies, relative to the experimental data in Figs. 2c and 2d. At low discharge rates, both mechanisms show a small, instantaneous drop in cell potential, followed by a concave-down transition between the upper and lower voltage plateaus, neither of which are typically observed in experimental data.

Comparing the discharge curves and polysulfide concentrations in Fig. 2 highlights the need for accurate species thermodynamics. For example, the discharge curve shape between the upper and lower voltage plateaus correlates with the intermediate polysulfide concentrations in ways that are both intuitive and instructive. Whereas the continuum-derived mechanisms (Figs. 2e and 2f) predict a transient $n = 6$ polysulfide (i.e., S_6^{2-} and Li_2S_6) peak followed by elevated $n = 4$ polysulfide concentrations, the atomistic models (Figs. 2g and 2h) predict persistent elevated Li_2S_6 and Li_2S_2 concentrations and negligible Li_2S_4. The $n = 6$ reduction in the continuum mechanisms provides a "bridge" between the upper and lower voltage plateaus, consistent with the gradual decrease in cell potential between the two. In contrast, all current in the atomistic mechanisms is produced via Li_2S_8 reduction until this species is consumed, at roughly 400 Ah kg_{sulfur}^{-1}. The cell potential drops suddenly, here, consistent with the Nernst potential for a reaction with vanishing reactant availability, until the cell potential reaches the lower-order polysulfide reduction potential.

Low-porosity simulations.—To explore mechanistic trends and cathode design in a more technologically-relevant context, the remaining simulation results assume cathode porosities ranging from 72.8–82.5%. We use these simulations to explore the differences between the "lithiated" and "non-lithiated" mechanisms in greater detail and to explore the influence of cathode design (namely the electrolyte to sulfur ratio) on battery performance and degradation. The porosity was adjusted by varying the initial sulfur loading, which in turn impacts the free electrolyte volume in the cathode, and subsequently the E/S ratio.

Comparing the lithiated and non-lithiated polysulfide mechanisms.—To compare the lithiated and non-lithiated polysulfide mechanisms, Fig. 3 shows discharge and polysulfide concentration profiles for both mechanisms at 1C and an initial cathode porosity of 82.5%. Figures 3a and 3b show the discharge curves, with the experimental data at 85% initial porosity overlaid solely to facilitate comparison to the Fig. 2 predictions. While the voltage curve of the non-lithiated mechanism is similar to that in Fig. 2a, the lithiated

Table IV. Kinetic parameters for the "lithiated polysulfide" mechanism in this work.

Reaction	Forward rate constant	Units
Sulfur/electrolyte interface		
$S_8(s) \rightleftharpoons S_8(e)$	1.9×10^{-2}[b]	—
Carbon/electrolyte interface		
$\frac{1}{2} S_8(e) + Li^+ + e^- \rightleftharpoons \frac{1}{2} Li_2S_8$	8.725×10^{16}[b]	kmol$^{-0.5}$ m$^{2.5}$ s^{-1}
$\frac{3}{2} Li_2S_8 + Li^+ + e^- \rightleftharpoons 2\, Li_2S_6$	4.331×10^{17}[b]	kmol$^{-1.5}$ m$^{5.5}$ s^{-1}
$Li_2S_6 + Li^+ + e^- \rightleftharpoons \frac{3}{2} Li_2S_4$	3.193×10^{15}[b]	kmol^{-1} m^4 s^{-1}
$\frac{1}{2} Li_2S_4 + Li^+ + e^- \rightleftharpoons Li_2S_2$	2.375×10^{12}[b]	kmol$^{-0.5}$ m$^{2.5}$ s^{-1}
$\frac{1}{2} Li_2S_2 + Li^+ + e^- \rightleftharpoons Li_2S(e)$	8.655×10^{13}[b]	kmol$^{-0.5}$ m$^{2.5}$ s^{-1}
Li_2S(s)/electrolyte interface		
$Li_2S(e) \rightleftharpoons Li_2S(s)$	1.075[b]	m s^{-1}
Li(s)/electrolyte interface		
$Li(s) \rightleftharpoons Li^+ + e^-$	3.0×10^{-8}[b]	kmol m^{-2} s^{-1}

a Assumed parameters. b fit parameters.

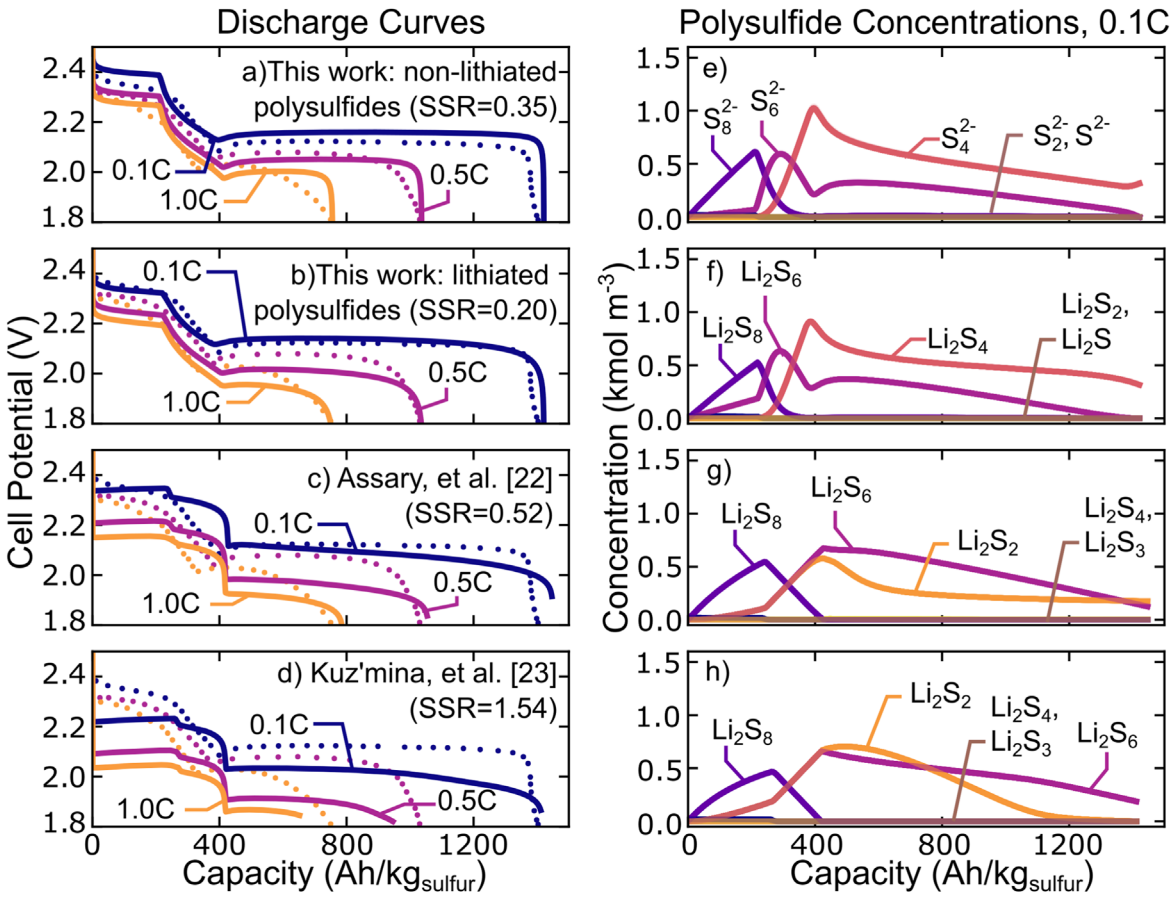

Figure 2. Discharge curves (a)–(d) and polysulfide concentrations (e)–(h) during discharge for four proposed Li-S mechanisms. Discharge curves are for rates of 0.1C, 0.5C, and 1C with a 85% porous cathode and 25 μm separator. Polysulfide concentrations are for discharge at 0.1C, demonstrating the impact of species thermodynamics on discharge phenomena. Simulated discharge curves (solid lines in (a)–(d)) are overlaid on experimental results (symbols) from Andrei et al.,[38] demonstrating close agreement for the continuum mechanisms developed as part of this work.

Table V. Model geometric parameters.

Parameter	Symbol	Value	Units
Number of cathode mesh volumes	n_{cat}	20	(–)
Number of electrolyte separator mesh volumes	n_{sep}	5	(–)
Number of anode mesh volumes	n_{an}	1	(–)
Cathode thickness	H_{cat}	100	μm
Electrolyte separator thickness	H_{sep}	25	μm
Cathode carbon specific surface area	a^{o}_{carbon}	2×10^4	$m^2_{carbon}\, m^{-3}_{cath}$

polysulfide mechanism predictions depart significantly from those in Fig. 2b. The upper plateau and transition region of Fig. 3b is similar to that of Fig. 2b; however, the lower plateau potential is significantly lower and loses some of its expected shape. This behavior is tied to the behavior of Li_2S_4, which reaches a maximum concentration of approximately 1.5 kmol m^{-3} and remains at this concentration, in contrast to the concentration profiles in Fig. 2f.

The polysulfide concentrations are shown in Figs. 3c and 3d and, as noted in Fig. 2, the discharge curve and concentration profile shapes are correlated. In particular, the upper voltage plateaus appear inversely related to the $n = 6$ polysulfide concentrations, and the lower voltage plateaus appear directly related to the $n = 6$ and inversely related to the $n = 4$ polysulfide concentrations. Each trace in Figs. 3c and 3d represents a different location (darker: cathode current collector and lighter: separator/anode interface). Concentration gradients are predicted for the non-lithiated polysulfides, beginning around 100–200 Ah/kg$_{sulfur}$, after $n = 6$ polysulfides are first produced in appreciable amounts. For the non-lithiated polysulfides, concentrations are higher in the separator than in the cathode, with relatively uniform concentrations throughout the cathode. For the lithiated polysulfides, concentration gradients are much smaller. Only Li_2S_8 concentrations shows noticeable gradients, with higher concentration in the cathode.

Predicted Li^+ ion concentrations in Fig. 4 help explain the polysulfide concentrations in Figs. 3c and 3d. The figure shows Li^+ concentration versus distance from the cathode current collector, with each trace representing a different discharge capacity (i.e. a different time during the 1C discharge). For the non-lithiated polysulfides (Fig. 4a), Li^+ concentration increases continuously throughout the cell until roughly 600 Ah kg$^{-1}_{sulfur}$, when Li_2S production decreases the overall Li^+ content. While Li precipitation is not explicitly modeled, the Li^+ concentration likely exceeds the saturation limit, further supporting the "lithiated polysulfide" pathway. For the lithiated polysulfides (Fig. 4b), the average Li^+

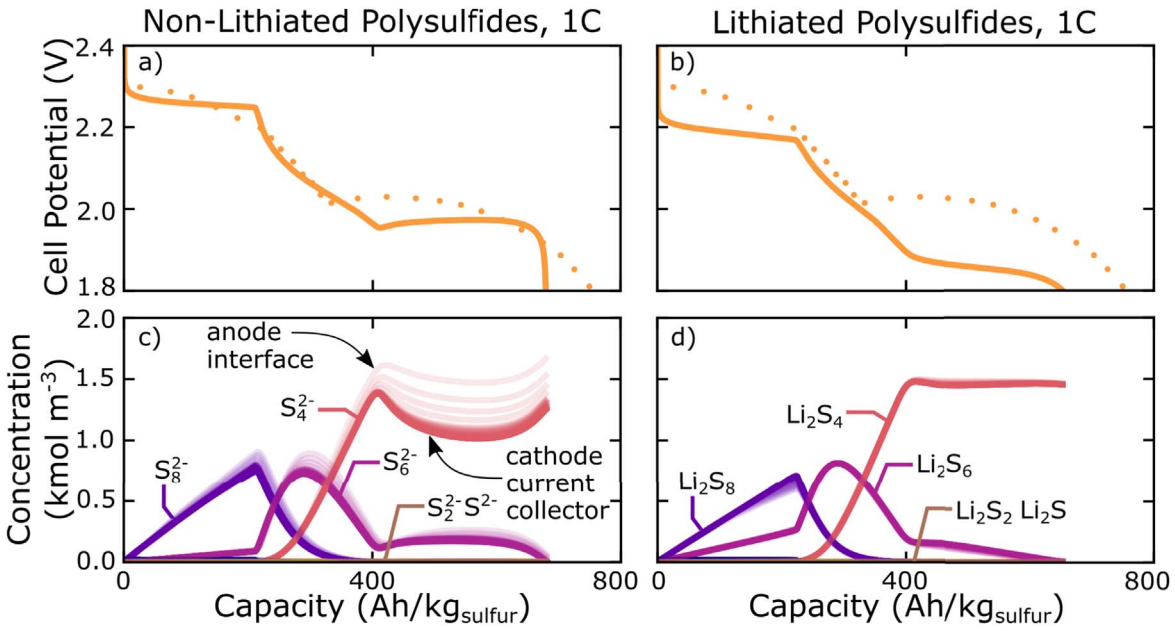

Figure 3. Discharge curves (a), (b) and polysulfide concentrations (c), (d) for the "non-lithiated" (a), (c) and "lithiated" (b), (d) polysulfide mechanisms during 1C discharge. Each polysulfide concentration trace represents a different location in the cell (lighter: closer to the separator/anode interface). Simulations included an initial porosity of 82.5%, an electrolyte/sulfur ratio of 4 μL mg^{-1}, and a nucleation density function of $n_m = 5 \times 10^{13} \exp(2.4221 \times C)$. Experimental data from Andrei et al., for cathodes with 85% porosity, are overlaid as symbols to facilitate comparison to Fig. 2.

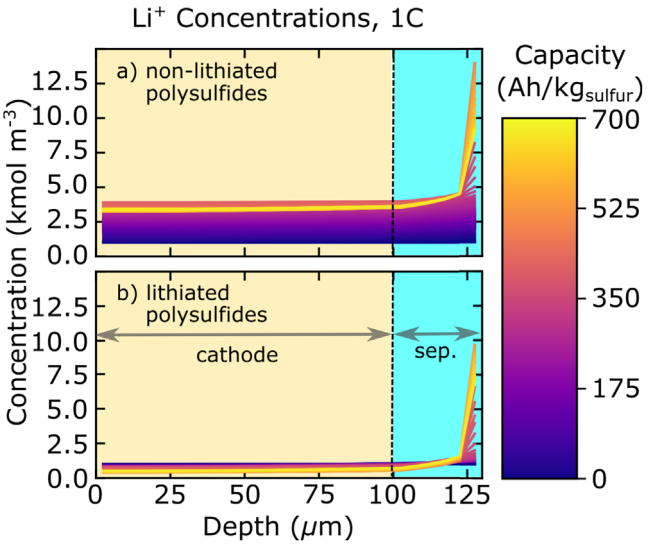

Figure 4. Electrolyte lithium ion concentration depth profiles for (a) "non-lithiated" and (b) "lithiated" polysulfide mechanisms during discharge at 1C, as shown in Fig. 3. Increases in the total Li^+ content for the non-lithiated mechanism maintain charge neutrality with increasing S_n^{2-} concentrations, while the overall Li^+ concentration for the lithiated mechanism remains constant. In both mechanisms, concentration gradients at the anode interface are due to increasing viscosity with increasing Li^+ (modeled here as decreasing D_{Li^+}), and decrease in magnitude near the end of discharge. Simulations included an initial porosity of 82.5%, an electrolyte/sulfur ratio of 4 μL mg^{-1}, and a nucleation density function of $n_m = 5 \times 10^{13} \exp(2.4221 \times C)$.

concentration remains constant. Moreover, the Li^+ concentration profile changes mostly at the beginning of discharge, quickly reaching a steady state that is maintained throughout discharge for most of the cell.

The differences here are explained by the assumption of charge neutrality and the role of Li^+ in the discharge processes for the two mechanisms. In the non-lithiated mechanism, Li^+ ions are not required for charge transfer. Rather, the Li^+ concentration increases to maintain charge neutrality, compensating for the polysulfide anion reduction products, S_n^{2-}. For the lithiated polysulfides, reduction reactions in the cathode consume Li^+ to form neutral Li_2S_n, rather than S_n^{2-}. Hence the total concentration of Li^+ cations in the cell remains constant as a function of time. The total lithium content of the cathode increases similar to Fig. 4a, but all excess lithium is in the form of lithiated polysulfides Li_2S_n, not Li^+. Moreover, Li_2S_n concentrations are not directly influenced by electric potentials or Li^+ concentration, and so the gradients in Fig. 3a are explained by diffusion to and from the separator, as polysulfide species are produced and consumed in the cathode.

At capacities of roughly 400–500 Ah kg$_{sulfur}^{-1}$, both mechanisms predict an increase in the Li^+ concentration at the anode interface and steep Li^+ concentration gradients in the separator. This is due to increasing electrolyte viscosity with increasing Li concentration, modeled here via lower D_{Li^+} in regions of higher Li concentration, as in Eq. 14. Lower D_{Li^+} values at the anode interface require higher concentration gradients to drive the required Li^+ flux toward the cathode. The S_n^{2-} gradients in the "non-lithiated" mechanism (Fig. 3c), are therefore explained by the Li^+ concentrations in Fig. 4a and the assumption of charge neutrality. The higher S_n^{2-} concentrations in the separator are proportional to the Li^+ concentration and occur at the same capacities where the largest Li^+ gradients are observed. As Li_2S is produced near the end of discharge, the overall Li content in the electrolyte decreases, and the Li^+ gradients reduce in magnitude.

Considering these results, along with *operando* measurements that observe lithiated polysulfides,[21] we recommend greater use of lithiated polysulfides in continuum-level simulations. Because the formation of ion pairs between the Li^+ and S_n^{2-} likely depends on the Li^+ availability, the dominant pathway is likely to shift during discharge, and fully accurate models should incorporate both pathways. This matches with Figs. 2a and 2b, where the two mechanisms each match the experimental data better in different regions. However, development of a combined mechanism will require significant input from atomistic models and chemically-resolved experimental validation data in order to estimate and fit the required

parameters. In general, it is difficult to hypothesize an exclusively "non-lithiated" mechanism. Thus, for the remainder of the present work we use the lithiated polysulfide mechanism to explore the effects of the battery electrolyte/sulfur ratio.

Cell design.—Performance metrics for consumer applications require lower Li-S battery volume and mass, typically achieved by reducing the electrolyte volume per unit mass of sulfur, known as the electrolyte/sulfur (E/S) ratio. Here, we explore the effects of cell design and operation for E/S ratios of 2, 3, and 4 μL mg_{sulfur}^{-1}. E/S ratios of 3 μL mg_{sulfur}^{-1} are common in state-of-the-art designs,[41] and exploring performance and electrolyte speciation in the neighborhood of this design can identify performance bottlenecks and degradation pathways to help inform next-generation battery designs. The simulations vary the E/S ratio by adjusting the areal sulfur loading, $m''^{,\circ}_{S_8}$, at a constant carbon volume fraction (i.e., porosity decreases with decreasing E/S ratio). The sulfur loading and cathode porosity for each E/S ratio, provided in Table VI, were chosen to match modern cathode designs, as provided in the "2021 Roadmap on lithium sulfur batteries"[10].

Figures 5a–5c show discharge curves for the three E/S ratios at rates of 0.1C, 0.5C, and 1C. Capacities are normalized relative to the single-cell battery mass (anode, separator, cathode, and liquid electrolyte), whereas the sulfur mass was used for Figs. 2 and 3. Gravimetric capacity increases with decreasing E/S from 4 to 3 μL mg^{-1} at 0.1C, consistent with the decrease in non-active material. With increasing C-rate, the lower E/S ratios predict losses associated with Li^+ transport limitations. The battery with E/S = 2 μL mg_{sulfur}^{-1} performs the worst of all cells, and never approaches full discharge. These E/S trends are consistent with results reported by Fan and Chiang.[9]

Figures 5d–5f show the polysulfide concentrations for the three E/S ratios at 1C. The polysulfide concentration profiles are similar for all three E/S ratios, but as expected, concentrations increase with decreasing E/S due to limited solvent availability to dilute the polysulfides. The impact of increasing electrolyte viscosity with decreasing electrolyte volume is clearly observed in Figs. 5e and 5f, where Li_2S_8 concentration gradients indicate preferential conversion to Li_2S_6 near the separator, due to the high Li^+ transport resistance through the cathode. Discharge for E/S = 2 and 3 μL mg_{sulfur}^{-1} terminates during periods of increasing Li_2S_n concentration, due to Li^+ starvation. Similar results are predicted for the "non-lithiated polysulfide" mechanism.

In addition to losses in power and energy performance, Figs. 5d–5f demonstrate that decreasing E/S ratios increase degradation risks associated with polysulfide precipitation.[9] The polysulfide concentrations increase with decreasing E/S ratio, and are uniformly higher than for Fig. 2b, which was run at an E/S ratio of approximately 5.4 μL mg_{sulfur}^{-1} and a rate of 0.1C. The concentrations in Figs. 5d and 5e approach the polysulfide solubility limits (e.g., 2 kmol m^{-3} for Li_2S_4.[38]) As discussed further below, care must be taken with new electrode and electrolyte approaches to prevent capacity fade via polysulfide precipitation.

Figure 6 plots energy versus power density (i.e. a Ragone plot) for 0.1C to 1C discharge, overlaid with a color plot of the maximum Li_2S_4 concentration during discharge, for E/S ratios of 2–4 μL mg_{sulfur}^{-1}. The energy and power densities were calculated as:

$$\text{Energy Density} = \frac{\int i V_{\text{cell}}\, dt}{3600 m_{\text{battery}}} \quad [22]$$

and:

$$\text{Power Density} = \frac{\int i V_{\text{cell}}\, dt}{t_{\text{discharge}}\ m_{\text{battery}}}, \quad [23]$$

where V_{cell} is the cell potential, m_{battery} is the mass per unit area, and $t_{\text{discharge}}$ is the total simulated time until the battery reached maximum discharge capacity. The Ragone plot shows tradeoffs between power and energy density with increasing C-rate, shown most clearly for E/S = 4 μL mg_{sulfur}^{-1}. Decreasing the E/S to 3 μL mg_{sulfur}^{-1} shows increased energy and power density below 0.3C, consistent with lower inactive material mass. For discharge rates greater than 0.2C, however, Li^+ transport becomes limiting, and the battery is unable to discharge completely, resulting in energy densities of roughly 150 Wh $kg_{battery}^{-1}$ or less. As observed in Fig. 5, the battery with E/S = 2 μL mg_{sulfur}^{-1} is unable to discharge completely at any C-rate modeled, and never achieves an energy density greater than 200 Wh $kg_{battery}^{-1}$. Again, this is related to the limited availability of solvent to dilute the dissolved polysulfides.

The Li_2S_4 concentrations demonstrate the risk of capacity fade due to polysulfide precipitation with high-performance cathodes. While the cell with E/S = 3 μL mg_{sulfur}^{-1} shows improved discharge performance up to 0.2C, Li_2S_4 concentrations approach their solubility limit (1.8 kmol m^{-3} vs 2.0 kmol m^{-3}, respectively), and may lead to precipitation in actual batteries, given spatially inhomogeneous electrolyte compositions in real cathode microstructures. Moreover, higher rate capability and lower E/S ratio are both associated with higher polysulfide concentrations, in Fig. 6. Better rate capability and low E/S ratio will both likely require limiting polysulfide dissolution. However, for any new designs that enable better performance by decoupling transport properties from polysulfide concentrations, polysulfide precipitation will become a concern.

Table VI. Cell design parameters for E/S study.

E/S Ratio (μL mg^{-1})	Sulfur Loading (mg cm^{-2})	Porosity (%)
4	2.45	82.5
3	3.17	79.1
2	4.46	72.8

Conclusions

In this paper, we present a 1D Li-S battery model which leverages the chemical kinetics software CANTERA to handle thermo-kinetic calculations in a robust, flexible, and generalized manner. This framework allows for easy comparison of Li-S mechanisms with arbitrary chemical complexity, to better understand and compare the limiting phenomena predicted by each. Given the chemical complexity of Li-S batteries, such a framework provides insight into mechanism aspects needed to capture key features in experimental data.

In this study, comparing four different mechanism candidates (two developed as part of this work, two derived from atomistic simulations) to experimental data yields key insights into mechanism development. For one, the reduction pathway can be written via lithiated or non-lithiated polysulfide intermediates. Results show that while the two mechanisms can reproduce quite similar discharge curves, they predict different polysulfide concentrations and corresponding limiting phenomena. Miller, et al.,[42] used X-ray spectromicroscopy to observe polysulfide concentrtion spatial distributions, and Schön and Krewer used cyclic voltammetry for insight into detailed reaction pathways.[20] These types of data could aid in providing further verification of proposed reaction pathways. While we conclude that a mechanism with purely lithiated polysulfides provides a better match to data than one based on purely non-lithiated polysulfides, ultimately both reaction pathways are likely important for predicting battery performance.[6]

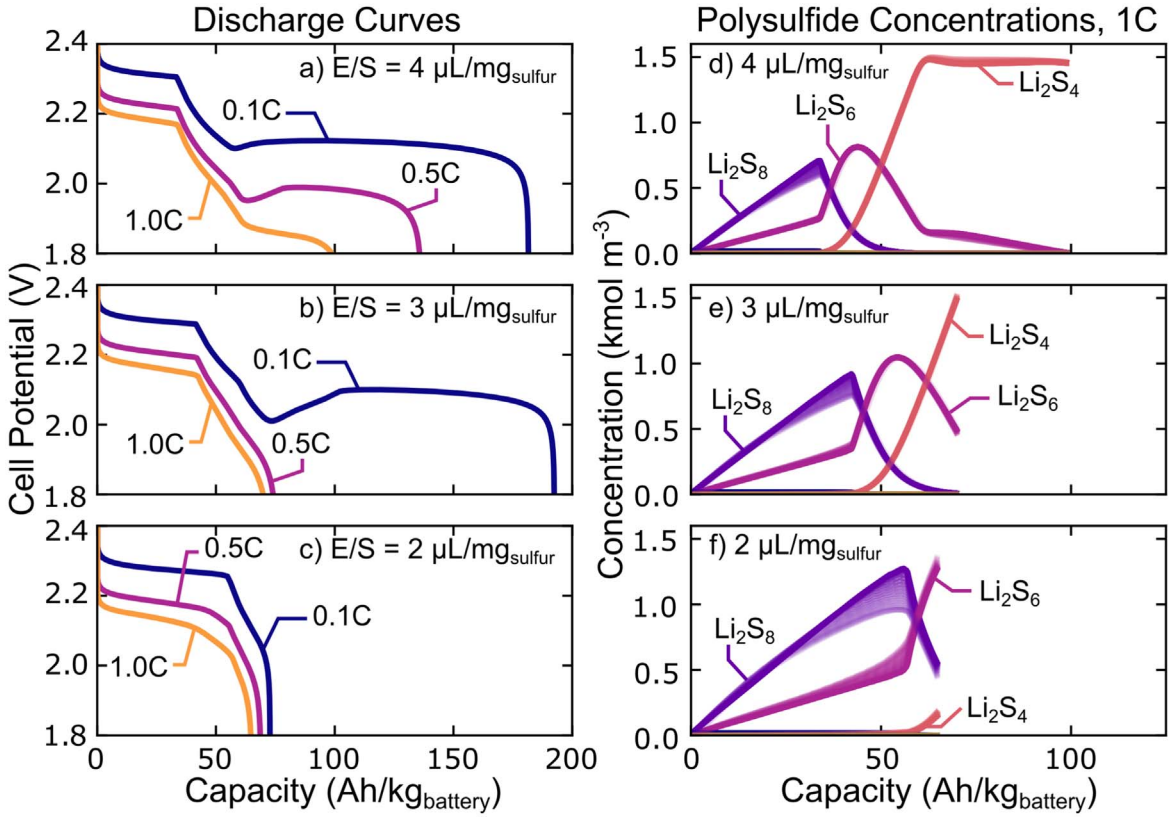

Figure 5. Discharge curves (a)–(c) and polysulfide concentrations (d)–(f) for three different electrolyte/sulfur ratios. Discharge curves are presented for 0.1C, 0.5C, and 1C discharge. Species concentrations for each E/S ratio are presented at 1C, with each trace representing a different location in the cell (lighter: closer to the electrolyte/anode interface).

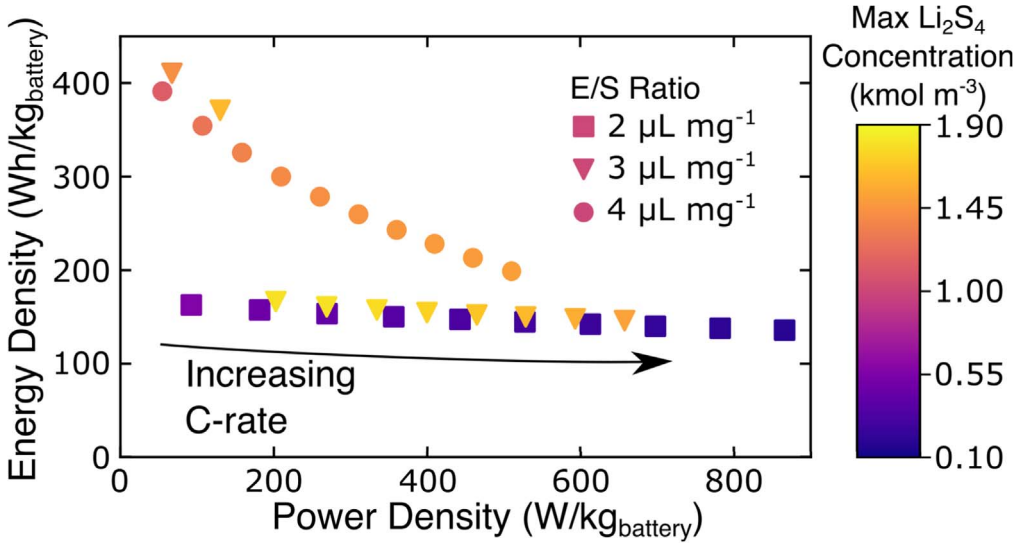

Figure 6. Ragone plot showing energy density vs power density of cells with electrolyte/sulfur ratios of 4 μL mg^{-1}, 3 μL mg^{-1}, and 2 μL mg^{-1}. Symbol colors represent the maximum concentration of Li_2S_4 during discharge. Discharge rages for all three E/S ratios begin at 0.1C, and increase in steps of 0.1C. The maximum C-rate is 1.0C for all E/S ratios.

Additionally, the model framework was used to explore the design and limitations of high-performance Li-S batteries via varying E/S ratio for varying discharge rates. The model performance predictions demonstrate the general challenge of balancing high energy and high power density in Li-S batteries. While low E/S batteries improve the energy density at low C-rates, performance degrades significantly at high C-rates due to Li^+ transport limitations, such that only marginal energy density (<200 Wh/kg) is recovered at high power. Moreover, viewing results through the lens of species concentrations demonstrates that polysulfides can exceed solubility limits at low E/S ratios, leading to capacity fade due to precipitation of polysulfide intermediates.

Considering Li-S cathode design more broadly, efforts to mitigate polysulfide shuttling by limiting polysulfide transport out of the cathode (e.g., via cation-selective separator coatings or restrictive cathode porosities) may encounter similar limitations due to the intermediate

polysulfide solubility. Continuum-level models to explore the design and operation space of Li-S batteries can therefore provide useful guidance to optimize the battery structure or composition for various applications. Simultaneously, further advances in understanding the intermediate thermo-kinetics in Li-S batteries are required to populate the necessary parameter sets for such detailed chemical modeling.

This work presents an initial effort to advance the chemical complexity in thermodynamically-reversible Li-S models, but still likely under-represents the actual degree of chemical complexity. As increasingly complex mechanisms are developed, populating the required model parameters (upwards of 50 thermodynamic and kinetic parameters in the present study) will require input from experiments and theoretical calculations. The challenge of adopting theoretical calculations for continuum-level models should not be dismissed. In this study, we implement two such mechanisms and find that performance predictions capture the major features of experimental observations, but miss some key details. Regardless, the results above demonstrate the value of detailed thermo-chemical modeling for Li-S battery design and analysis. Incorporating parallel lithiated and non-lithiated polysulfide pathways, for example, will likely reduce the predicted polysulfide concentrations, relative to either pathway in isolation. This, in turn, can help identify favorable battery designs and/or operating strategies for Li-S battery designs that leverage the promise of the chemistry's potential for cheap, portable, efficient, and environmentally benign energy storage.

Acknowledgments

Work at the Colorado School of Mines was funded in part by NSF Award 1 931 584, Program Manager S. Park. This work was authored in part by Alliance for Sustainable Energy, LLC, the manager and operator of the National Renewable Energy Laboratory for the U.S. Department of Energy (DOE) under Contract No. DE-AC36-08GO28308. Funding was provided by the U.S. DOE Office of Vehicle Technologies Energy Storage Program, Computer-Aided Engineering of Batteries program manager Brian Cunningham. The views expressed in the article do not necessarily represent the views of the DOE or the U.S. Government. The U.S. Government retains and the publisher, by accepting the article for publication, acknowledges that the U.S. Government retains a nonexclusive, paid-up, irrevocable, worldwide license to publish or reproduce the published form of this work, or allow others to do so, for U.S. Government purposes.

ORCID

Daniel Korff https://orcid.org/0000-0001-7070-8256
Andrew M. Colclasure https://orcid.org/0000-0002-9574-5106
Yeyoung Ha https://orcid.org/0000-0003-2679-2539
Kandler A. Smith https://orcid.org/0000-0001-7011-0377
Steven C. DeCaluwe https://orcid.org/0000-0002-3356-8247

References

1. X. Q. Zhang, C. Z. Zhao, J. Q. Huang, and Q. Zhang, *Engineering*, **4**, 831 (2018).
2. D. N. Fronczek and W. G. Bessler, *J. Power Sources*, **244**, 183 (2013), 16th International Meeting on Lithium Batteries (IMLB).
3. M. Wild, L. O'Neill, T. Zhang, R. Purkayastha, G. Minton, M. Marinescu, and G. J. Offer, *Energy Environ. Sci.*, **8**, 3477 (2015).
4. J. Brückner, S. Thieme, H. T. Grossmann, S. Dörfler, H. Althues, and S. Kaskel, *J. Power Sources*, **268**, 82 (2014).
5. J. Akridge, Y. Mikhaylik, and N. White, *Solid State Ionics*, **175**, 243 (2004).
6. N. Kamyab, P. T. Coman, S. K. M. Reddy, S. Santhanagopalan, and R. E. White, *J. Electrochem. Soc.*, **167**, 130532 (2020).
7. A. N. Mistry and P. P. Mukherjee, *J. Phys. Chem. C*, **122**, 7 (2018).
8. T. Zhang, M. Marinescu, L. O'Neill, M. Wild, and G. Offer, *Phys. Chem. Chem. Phys.*, **17**, 22581 (2015).
9. F. Y. Fan and Y. M. Chiang, *J. Electrochem. Soc.*, **164**, A917 (2017).
10. J. B. Robinson et al., *J. Phys.: Energy*, **3**, 031501 (2021).
11. H. Chen et al., *Matter*, **2**, 1605 (2020).
12. M. Liu, F. Ye, W. Li, H. Li, and Y. Zhang, *Nano Research*, **9**, 94 (2016).
13. Z. Cheng, H. Pan, J. Chen, X. Meng, and R. Wang, *Adv. Energy Mater*, **9**, 1901609 (2019).
14. Q. Pang, J. Tang, H. Huang, X. Liang, C. Hart, K. C. Tam, and L. F. Nazar, *Adv. Mater.*, **27**, 6021 (2015).
15. K. Kumaresan, Y. Mikhaylik, and R. E. White, *J. Electrochem. Soc.*, **155**, A576 (2008).
16. Y. Ren, T. Zhao, M. Liu, P. Tan, and Y. Zeng, *J. Power Sources*, **336**, 115 (2016).
17. T. Danner and A. Latz, *Electrochimica Acta*, **322**, 134719 (2019).
18. T. Zhang, M. Marinescu, S. Walus, and G. J. Offer, *Electrochimica Acta*, **219**, 502 (2016).
19. A. F. Hofmann, D. N. Fronczek, and W. G. Bessler, *J. Power Sources*, **259**, 300 (2014).
20. P. Schön and U. Krewer, *Electrochimica Acta*, **373**, 137523 (2021).
21. N. Saqib, G. M. Ohlhausen, and J. M. Porter, *J. Power Sources*, **364**, 266 (2017).
22. R. S. Assary, L. A. Curtiss, and J. S. Moore, *The Journal of Physical Chemistry C*, **118**, 11545 (2014).
23. E. V. Kuz'mina, E. V. Karaseva, N. V. Chudova, A. A. Mel'nikova, and V. S. Kolosnitsyn, *Russ. J. Electrochem.*, **55**, 978 (2019).
24. L. Kong, L. Yin, F. Xu, J. Bian, H. Yuan, Z. Lu, and Y. Zhao, *J. Energy Chem.*, **55**, 80 (2021).
25. E. Karaseva, E. Kuzmina, D. Kolosnitsyn, N. Shakirova, L. Sheina, and V. Kolosnitsyn, *Electrochimica Acta*, **296**, 1102 (2019).
26. G. Bieker, J. Wellmann, M. Kolek, K. Jalkanen, M. Winter, and P. Bieker, *Phys. Chem. Chem. Phys.*, **19**, 11152 (2017).
27. A. Gupta, A. Bhargav, and A. Manthiram, *Adv. Energy Mater*, **9** (2019).
28. C. D. Parke, A. Subramaniam, V. R. Subramanian, and D. T. Schwartz, *ChemElectroChem*, **8**, 1098 (2021).
29. V. Thangavel, A. Mastouri, C. Guéry, M. Morcrette, and A. A. Franco, *Batteries & Supercaps*, **4**, 152 (2020).
30. J. P. Neidhardt, D. N. Fronczek, T. Jahnke, T. Danner, B. Horstmann, and W. G. Bessler, *J. Electrochem. Soc.*, **159**, A1528 (2012).
31. D. G. Goodwin, R. L. Speth, H. K. Moffat, and B. W. Weber, *Cantera: An Object-oriented Software Toolkit for Chemical Kinetics, Thermodynamics, and Transport Processes* https://www.cantera.org Version 2.4.0 (2018).
32. G. Van Rossum and F. L. Drake, *Python 3 Reference Manual* (CreateSpace, Scotts Valley, CA) (2009).
33. C. Andersson, C. Führer, and J. Åkesson, *Math. Comput. Simul.*, **116**, 26 (2015).
34. S. C. DeCaluwe, P. J. Weddle, H. Zhu, A. M. Colclasure, W. G. Bessler, G. S. Jackson, and R. J. Kee, *J. Electrochem. Soc.*, **165**, E637–58 (2018).
35. B. Tjaden, S. J. Cooper, D. J. Brett, D. Kramer, and P. R. Shearing, *Curr. Op. Chem. Eng.*, **12**, 44 (2016).
36. C. Kupper and W. G. Bessler, *J. Electrochem. Soc.*, **164**, A304–20 (2016).
37. A. N. Mistry and P. P. Mukherjee, *J. Phys. Chem. C*, **122**, 18329 (2018).
38. P. Andrei, C. Shen, and J. P. Zheng, *Electrochimica Acta*, **284**, 469 (2018).
39. Korff D and DeCaluwe S C Lithium-Sulfur 1D Model, https://github.com/coresresearch/LiS-Battery/tree/publication.
40. Korff D, Colclasure A M, Ha Y, Smith K A and DeCaluwe S C Pathways toward high-energy li-sulfur batteries, identified via multi-reaction chemical modeling: Manuscript repository, https://github.com/coresresearch/Li-Sulfur-Modeling-Paper.
41. K. Ning, Y. Lin, L. Yang, D. Lu, J. Xiao, Y. Qi, and M. Cai, *Nat. Commun.*, **10** (2019).
42. E. C. Miller, R. M. Kasse, K. N. Heath, B. R. Perdue, and M. F. Toney, *J. Electrochem. Soc.*, **165**, A6043 (2017).